

Exploring quantum signatures of chaos on a Floquet synthetic latticeEric J. Meier,^{*} Jackson Ang'ong'a,^{*} Fangzhao Alex An, and Bryce Gadway[†]*Department of Physics, University of Illinois at Urbana-Champaign, Urbana, Illinois 61801-3080, USA*

(Received 20 May 2019; published 19 July 2019)

Ergodicity and chaos play an integral role in the behavior of dynamical systems and are crucial to the formulation of statistical mechanics. Still, a general understanding of how ergodicity and chaos emerge in the dynamical evolution of closed quantum systems remains elusive. Here, we develop an experimental platform for the realization of canonical quantum chaotic Hamiltonians based on quantum simulation with synthetic lattices. We map the angular momentum projection states of an effective quantum spin onto the linear momentum states of a ⁸⁷Rb Bose-Einstein condensate, which can be alternatively viewed as synthetic lattice sites. This synthetic lattice, with local and dynamical control of tight-binding lattice parameters, enables new capabilities related to the experimental study of quantum chaos. In particular, the capabilities of our system let us tune the effective size of our spin, allowing us to illustrate how classical chaos can emerge from a discrete quantum system. Moreover, spectroscopic control over our synthetic lattice allows us to explore unique aspects of our spin's dynamics by measuring the out-of-time-ordered correlation function and enables future investigations into new symmetry classes of chaotic kicked-top systems.

DOI: [10.1103/PhysRevA.100.013623](https://doi.org/10.1103/PhysRevA.100.013623)**I. INTRODUCTION**

The contrasting behavior of quantum and classical systems is most apparent in their nonlinear dynamical response to a periodic drive [1]. While driven classical systems can play host to truly chaotic behavior, including the loss of information about specific initial conditions, it is expected that true memory loss will not occur in closed and bounded quantum systems [2]. This stems from both the unitary nature of closed quantum systems, which strictly forbids memory loss, and the relevance of quantum uncertainty and the effective smearing of phase space in small quantum systems. This smearing of states in phase space dulls the sensitivity to initial conditions encountered in classically chaotic systems. Over the past few decades a number of experimental systems have illustrated this stark contrast between the nonlinear dynamics of classical and quantum systems, e.g., the spectra of atoms in applied electromagnetic fields [3,4], the response of cold-matter waves to time-periodic optical lattices [5–9], and the scattering of complex atoms and molecules in an applied field [10,11].

The kicked-top model, in which the symmetry of a precessing spin is broken by a series of nonlinear “kicks” [1], is one of the most paradigmatic systems giving rise to chaotic behavior. The correspondence between the nonlinear dynamics of classical and quantum systems has been explored through several experimental realizations [12–14] of quantum kicked-top models, where the spin is quantized with a finite angular momentum value J . In a pioneering exploration of chaotic phenomena in quantum systems, Ref. [12] studied the dynamics of the ground hyperfine manifold ($F = 4$) of thermal

cesium atoms. The atoms were subjected to a continuous nonlinear twist realized through a state-dependent light shift of the magnetic sublevels m_F and a periodic linear kick given by a transverse magnetic field. While such studies could be extended to slightly smaller or larger spins with different atomic species or Rydberg atoms [15], a more flexible approach to designing effective spins with tunable size has recently been realized. Using spectrally resolved addressing of transitions in a multilevel superconducting qudit, Ref. [13] demonstrated the engineering of artificial spin- J systems and control over linear rotations.

Here, in the spirit of creating synthetic spins through coherent control, we engineer a highly tunable momentum-space lattice [16,17] with full control over the tunneling and site-energy landscapes. In our approach, the momentum states of a $(2J + 1)$ -site lattice play the role of angular momentum sublevels $m_J \in \{-J, J\}$ [see Fig. 1(a)], enabling natural control over the size of the spin J . This simple control over J allows us to study the crossover from a highly quantum regime (small J), where chaotic behavior is mostly suppressed, towards the nearly classical limit (moderate to large J), where chaotic behavior is predicted to emerge.

A. Kicked-top model

The dynamics of the kicked-top system are captured by the time-dependent Floquet Hamiltonian

$$H(\tau) = \frac{\rho}{T} J_x + \frac{\kappa}{2J} J_z^2 \sum_N \delta(\tau - NT), \quad (1)$$

where the first term represents continuous rotation about the x axis at a rate ρ/T and the second describes a train of effectively instantaneous torsional J_z^2 kicks of strength κ spaced by a period T , with N being the kick number and τ being the time variable. In the classical limit, symmetry

^{*}These authors contributed equally to this work.[†]bgadway@illinois.edu

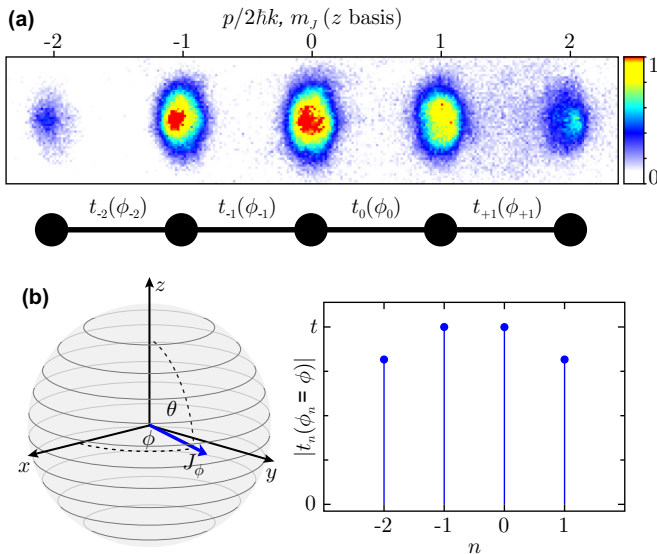


FIG. 1. Experimental scheme. (a) Time-of-flight absorption image (top) and cartoon (bottom) depicting a $J = 2$ lattice where the lattice sites represent the angular momentum sublevels m_j . (b) Arbitrary torque vector on the equator of the Bloch sphere (left) emulated in this system through the tunneling links $|t_n(\phi_n = \phi)|$ (right).

breaking by the J_z^2 kicks gives rise to chaotic dynamics for certain initial orientations of the spin, with islands of stability in phase space for moderate nonlinear coupling. As κ is increased, the onset of global chaos leads to the loss of all stable, regular trajectories of the spin. In the limit of small J , the lack of well-defined spin orientations due to quantum uncertainty results in a general insensitivity to initial conditions and a suppression of chaotic behavior. Specifically, it dulls the sensitivity to initial conditions found in the classical Hamiltonian dynamics.

Connections between classical chaos and the generation of quantum entanglement [18,19] add further interest to the interplay between classical and quantum dynamics. For quantum kicked-top dynamics in which the spin- J object represents the collective spin of many interacting spin-1/2 particles (e.g., in atomic condensates with a spin degree of freedom [14]) scenarios leading to classical chaos can generate quantum correlations and metrologically useful spin squeezing [20]. Starting from a coherent spin state (CSS), the states of the individual particles become entangled, and the many-body state becomes nonseparable under the evolution of Eq. (1). The direct measurement of multiparticle correlations generated by kicked-top dynamics has recently been achieved for the small- J limit, in a system of superconducting qubits with engineered interactions [21].

Here, instead of studying the collective spin of many interacting spin-1/2 particles, we directly mimic the dynamics of a single spin- J quantum object. To successfully explore quantum chaos in this system, we must be able to engineer an effective spin system, realize the kicked-top Hamiltonian of Eq. (1), accurately prepare initial states of the spin, and measure the final state of the spin after some dynamical evolution. In the following sections, we describe how we achieve these tasks using momentum-space lattice techniques.

B. The momentum-space lattice as a synthetic spin

Our momentum-space lattice is created from two counter-propagating laser beams with a nearly common wavelength $\lambda = 1064$ nm and wave vector $k = 2\pi/\lambda$. One of the beams has only a single frequency component, while its counterpropagating partner contains multiple discrete frequency components. Initially at rest, the atoms transition between discretized momentum states $p_n = 2n\hbar k$ (separated by twice the photon recoil momentum) by exchanging photons between the two laser beams. That is, the atoms undergo a Bragg diffraction process where they are virtually excited by a photon from one laser beam and then emit a photon into the counterpropagating beam via stimulated emission, resulting in a $\pm 2\hbar k$ momentum change. The frequencies of the many components of the multifrequency laser are chosen to match different two-photon Bragg resonance conditions, creating a set of resonantly connected momentum states that serve as the sites of the momentum-space lattice. By careful tuning of the number, frequency, amplitude, and phase of the components of the multifrequency beam, we exert full control over the number of sites, site energies, tunneling strengths, and tunneling phases in our lattice, respectively [22]. During an 18-ms time-of-flight expansion period at the end of every experimental cycle, the atoms at different sites of the lattice naturally separate from each other according to their momenta, which allows us to perform site-resolved measurements through standard absorption imaging.

We engineer an artificial spin and realize dynamics governed by Eq. (1) by coupling many discrete momentum states in a controlled and time-dependent fashion as described above. By mapping the z -basis projections of the spin, i.e., the m_j sublevels, onto the momentum states in our lattice, the two terms of Eq. (1) allow for a simple realization in terms of lattice dynamics. The J_x rotation can be viewed as a kinetic evolution enabled by tunneling (undergoing Bragg diffraction) between adjacent sites. The nonlinear J_z^2 kicks are simply instantaneous site-dependent phase shifts, or, alternatively, represent evolution without tunneling for a fixed time in a quadratic potential of site energies. We realize these elementary processes in a one-dimensional momentum-space lattice [16,17] populated by atoms from a ^{87}Rb Bose-Einstein condensate, as depicted in the time-of-flight absorption image shown in Fig. 1(a).

C. Linear spin operators: Rotations

The linear spin operator J_x (J_y) can be visualized as the rotation of a given spin state about a torque vector lying on the equator ($\theta = \pi/2$) of the Bloch sphere. A CSS $|\theta, \phi\rangle$ can easily be visualized on the Bloch sphere as well, where the spin is oriented along the polar and azimuthal angles θ and ϕ , respectively. While interactions lead to no significant correlated behavior in our system, which is rather based on the direct emulation of a spin- J object, this language of a spin on the Bloch sphere provides for an intuitive picture of the system dynamics. Alternatively, J_x and J_y can be understood as the matrix representations of the magnetic dipole operator between different $|J, m_j\rangle$ states in a transverse magnetic field.

In order to implement generic rotations about equatorial torque vectors pointing along any azimuthal angle ϕ , i.e., $J_\phi =$

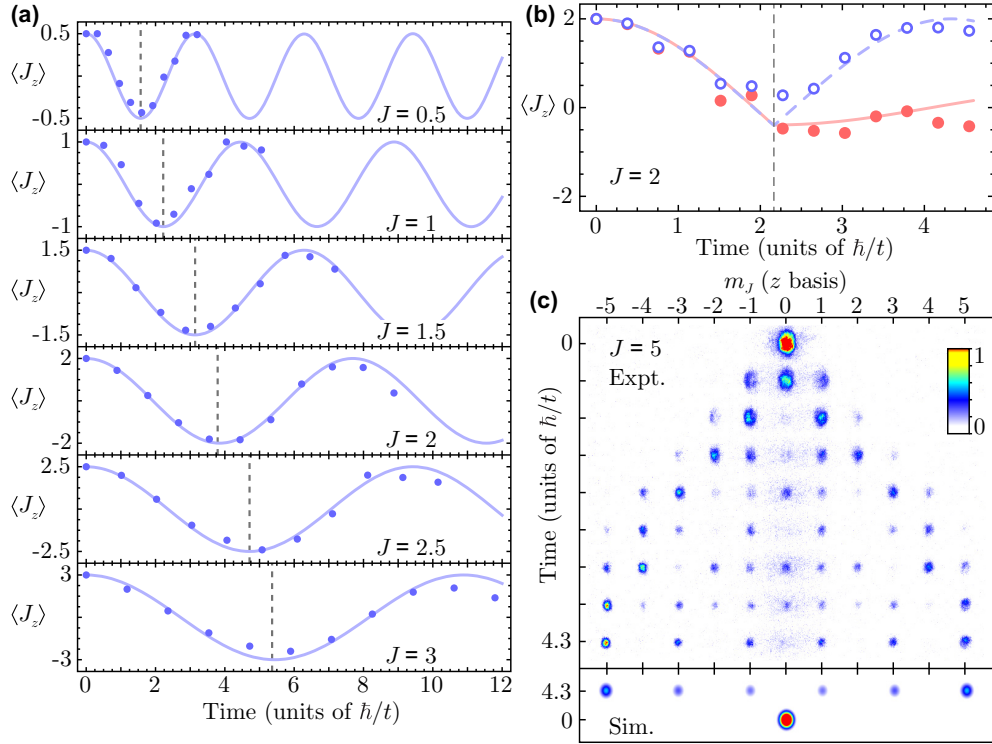


FIG. 2. Demonstrations of linear rotations. (a) Evolution of $\langle J_z \rangle$ for several spin sizes starting in $|\theta = 0, \phi = 0\rangle_{\text{CSS}}$ and evolving under a J_x operator. The solid blue lines are results from simulations of Eq. (3) with no free parameters, and the dashed gray lines show the theoretical π pulse times. (b) Expectation value $\langle J_z \rangle$ for a spin-2 state evolving under a J_x operation until the gray dashed line at $\approx 2.2 \hbar/t$. At this time, the operation is switched to either J_{-y} (red dots and solid red theory line) or J_{-x} (open blue dots and dashed blue theory line). (c) Top: Experimental absorption images showing the evolution of a $J = 5$ spin starting in $|J = 5, m_J = 0\rangle_z$ evolving under a $-J_y$ operator. Bottom: Simulated absorption images showing the final atomic distribution and the initial state $|J = 5, m_J = 0\rangle_z$. All error bars are one standard error of the mean. The error bars represent only statistical errors and are not visible because they are smaller than the data markers.

$J_x \cos(\phi) + J_y \sin(\phi)$, we tailor the tunneling amplitudes and phases between adjacent lattice sites as depicted in Fig. 1(b). We introduce tunneling terms $t_n(\phi_n)$ linking lattice site n to site $n + 1$ (or, equivalently, angular momentum state m_J to $m_J + 1$) with tunneling phase ϕ_n , taking the form of the matrix elements of the desired spin operator:

$$t_n(\phi_n) = A\sqrt{J(J+1) - n(n+1)}e^{i\phi_n}. \quad (2)$$

Here, $n \in \{-J, J-1\}$ is the tunneling term index representing a drive field linking momentum states n and $n + 1$, and A is a constant with units of energy related to the tunneling rate. This tunneling function has a maximum amplitude at the center of the m_J manifold, which we label t for convenience [see Fig. 1(b)]. Using these tunneling links, we simulate the tight-binding Hamiltonian

$$H_{\text{tb}}(\phi_n) = \sum_{n=-J}^{J-1} [t_n(\phi_n)c_{n+1}^\dagger c_n + \text{H.c.}], \quad (3)$$

where c_n^\dagger (c_n) creates (annihilates) a particle at site n . The tunneling phase ϕ_n determines the direction of the effective torque vector in the x - y plane, where J_x and J_y relate to $H_{\text{tb}}(\phi_n = 0)$ and $H_{\text{tb}}(\phi_n = \pi/2)$, respectively.

Figure 2 summarizes our ability to perform these linear, equatorial spin rotations. Beginning from stretched state $|J, m_J = J\rangle$, we monitor the z -axis projection of the spin evolving under a J_x operator for several values of J [Fig. 2(a)].

The observed dynamics are in good agreement with theory, with the observed times of spin inversion (π -pulse times) matching well with theoretical predictions (dashed lines) for varying J [23].

We further illustrate our phase- and time-dependent control over spin operations in Fig. 2(b). For an initial spin state $|J = 2, m_J = 2\rangle$, we first apply a J_x rotation for a time corresponding to a $\pi/2$ pulse. We then modify our tunneling parameters to instantly change the direction of the effective torque vector. For a complete inversion of the torque vector to $-J_x$ [evolution under $H_{\text{tb}}(\pi)$, open blue circles], we find that the dynamics of the spin reverse towards the initial state. If we instead shift the torque vector to $-J_y$ [evolution under $H_{\text{tb}}(-\pi/2)$, red solid circles], we find that the dynamics essentially cease since the spin is aligned along the new torque vector. Continued evolution of the spin as seen in Fig. 2(b) is due to the spin having rotated further than desired prior to the sudden shift of the torque vector.

D. State preparation

As demonstrated in Figs. 2(a) and 2(b), we are able to prepare our spin in the stretched state $|J, m_J = J\rangle$ by a simple definition of the synthetic lattice site index with respect to the discrete momentum values ($m_J = J + p/2\hbar k$) and a corresponding choice of the applied Bragg resonance frequencies. We can furthermore initiate the spin in any state

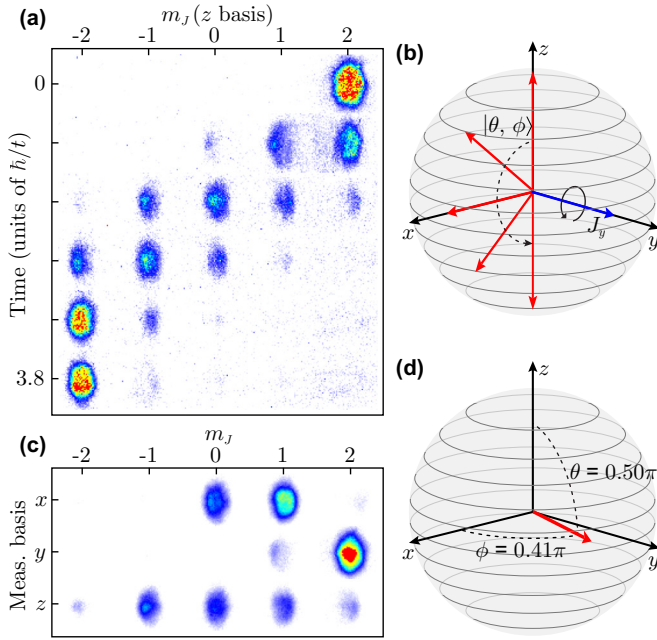


FIG. 3. State preparation and measurement. (a) Absorption images (in the z basis) of a $J = 2$ spin rotating from $|\theta = 0, \phi = 0\rangle_{\text{CSS}}$ to $|\theta = \pi, \phi = 0\rangle_{\text{CSS}}$ under a J_y operator. (b) Bloch sphere representation of the state rotation shown in (a). The state vector is depicted by the red arrows, and the J_y operator is depicted by the blue arrow. (c) Images (averaged over many shots) of a $J = 2$ spin in the state $|\theta = 0.50\pi, \phi = 0.41\pi\rangle_{\text{CSS}}$ as measured along the x , y , and z bases. (d) Bloch sphere depiction of the measured vector shown in (c).

with well-defined angular momentum in the z basis $|J, m_J\rangle$ by simply defining the corresponding site of our synthetic lattice to match our zero-momentum condensate. These initial states with $m_J \neq \pm J$ would represent states that are squeezed with respect to the operators J_x , J_y , and J_z [24]. While there are no significant correlations between the atoms in these experiments, the ability to prepare arbitrary initial states of our synthetic spin does allow us to explore the evolution of squeezed states under a classically chaotic Hamiltonian. Figure 2(c) shows the evolution of the state $|J = 5, m_J = 0\rangle$ under a $-J_y$ spin rotation. This angular momentum state displays interesting dynamics as it is rotated. For example, when measured after a $\pi/2$ rotation (an evolution time of $\sim 4.3\hbar/t$) a highly modulated m_J distribution is observed, in excellent agreement with a direct numerical simulation (bottom plot).

In addition to states with definite m_J , we may also prepare coherent states pointed in any direction $|\theta, \phi\rangle$. To prepare such a state, we start by initializing our atoms at the north pole of the Bloch sphere, i.e., $m_J = J$. Since this state is equivalent to $|\theta = 0, \phi = 0\rangle_{\text{CSS}}$, we can apply a rotation of the spin to transform it to any coherent state. In the following experiments we create arbitrary states with parameters $|\theta_i, \phi_i\rangle$ by applying tunneling links $t_n(\phi_i + \pi/2)$ for a time corresponding to a θ_i pulse. This takes the initial state, which is aligned at the north pole of the Bloch sphere, down along a constant azimuthal angle ϕ_i to a polar angle θ_i , thus preparing the CSS $|\theta_i, \phi_i\rangle$. Figure 3(a) shows a series of time-of-flight absorption images illustrating this procedure. The atoms start in $m_J = 2$ and

make their way to $m_J = -2$ during the pulse duration. The schematic of this procedure on the Bloch sphere is shown in Fig. 3(b), where the state vector (red arrows) rotates about a J_y operator (blue arrow) from $|\theta = 0, \phi = 0\rangle_{\text{CSS}}$ to $|\theta = \pi, \phi = 0\rangle_{\text{CSS}}$.

E. State measurement

One nice feature of momentum-space lattices is the straightforward ability to measure population at each lattice site directly through time-of-flight absorption imaging. In the context of studying the dynamics of an effective spin- J particle on a $(2J + 1)$ -site lattice, this relates to directly measuring the m_J state distribution in the z basis. Further information about the quantum state of this artificial spin can be accessed by measuring the spin projection along alternative spin axes, i.e., along the J_x and J_y spin directions. We perform these measurements, related to measuring the coherences between z -basis states, by applying a linear rotation about a chosen torque vector prior to z -basis imaging. That is, to measure along the x (y) axis we apply a $-J_y$ (J_x) rotation for a time corresponding to a $\pi/2$ pulse prior to time-of-flight absorption imaging. Figure 3(c) shows a particular CSS as measured in the x , y , and z spin bases, while Fig. 3(d) shows the reconstructed state vector on the Bloch sphere, relating to mean values $\langle J_x \rangle$, $\langle J_y \rangle$, and $\langle J_z \rangle$ of this separable CSS [25].

F. Nonlinear kick operation

To realize the kicked-top model, we additionally need to implement a nonlinear J_z^2 kick. In the context of collective spin states [20], where such a nonlinear spin operation is derived from direct interactions (such as in multimode condensates with mode-dependent interactions [14] or through the collective, long-range interactions of many ions [26]) or field-mediated interactions (such as for atoms in optical cavities [27]), such a term gives rise to the buildup of correlations and entanglement between the constituent particles.

In experiments such as ours that are directly based on effectively spin- J particles [12], the J_z^2 kick term relates instead to engineering a quadratic, m_J -dependent phase shift to the z -basis magnetic sublevels, creating nontrivial phase differences between adjacent m_J states that impact their further evolution under subsequent linear rotations. For the case of emulating an artificial spin within a synthetic lattice of states, such a J_z^2 kick can be created through application of a quadratic potential of the site energies in the absence of tunneling.

Alternatively, we directly engineer effective instantaneous relative phases at the different m_J sites. This is accomplished by suddenly shifting the tunneling phase between two adjacent m_J states to reflect the phase difference acquired during the instantaneous J_z^2 kick. This approach is unique to systems based on driven tunneling, which allow phase-dependent control of tunneling. As a concrete example for $J = 2$, a J_z^2 kick with $\kappa = \pi/8$ leads to a relative phase accrual of $3\pi/8$ between the states $m_J = 1$ and $m_J = 2$. In our system, this phase difference is implemented by instantaneously shifting the phase of the $m_J = 1 \rightarrow m_J = 2$ tunneling link as $t_1(\phi_1) \rightarrow t_1(\phi_1 + 3\pi/8)$ or, more generally, $\phi_n \rightarrow \phi_n + (2n + 1)\kappa$ for the $n \rightarrow n + 1$ tunneling phase.

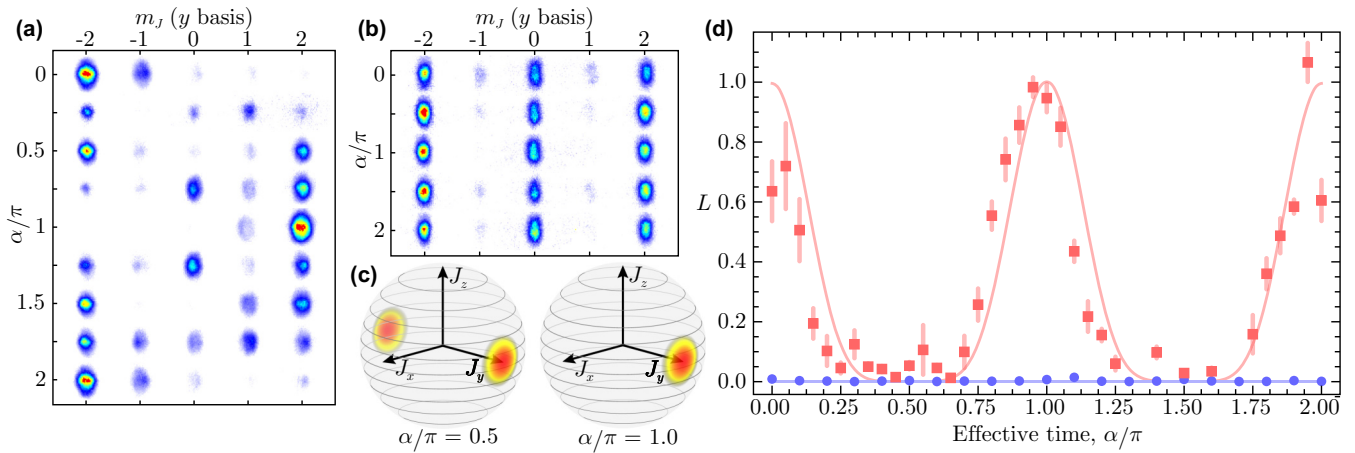


FIG. 4. Squeezing of the artificial spin. Absorption images of the y -basis spin projection as a function of the effective squeezing time α when starting in (a) $|\theta = \pi/2, \phi = -\pi/2\rangle_{\text{CSS}}$ and (b) $|J = 2, m_J = 0\rangle_z$. (c) Density distributions for initial state $|\theta = \pi/2, \phi = -\pi/2\rangle_{\text{CSS}}$ shown at effective times $\alpha/\pi = 0.5$ (left) and $\alpha/\pi = 1.0$ (right). (d) Spin length L versus the effective squeezing time α . The red squares and simulation line are for initial state $|\theta = \pi/2, \phi = -\pi/2\rangle_{\text{CSS}}$, and the blue dots and simulation line are for $|J = 2, m_J = 0\rangle_z$. All error bars are one standard error of the mean.

II. RESULTS

A. Nonlinear dynamics of the artificial spin

We first examine the dynamics of our artificial spin under evolution governed by an effective squeezing Hamiltonian $H_{\text{sq}} = \alpha_0 J_z^2$. For any initial state, the m_J population distribution will be unaffected in the z basis. Therefore, to explore the influence of the J_z^2 term, we measure the x and y spin distributions by rotating into these measurement bases. The phase accrual of the z -basis m_J states is accounted for by an appropriate modification of the phase terms of the various tunneling elements used to rotate the spins for measurement of J_x and J_y .

For certain initial states $|\theta, \phi\rangle$, evolution under H_{sq} leads to the generation of correlations in the uncertainty of the spin value along the x , y , and z directions. With increasing evolution time, the spin distribution undergoes periodic cycles of becoming squeezed (having reduced spread along one spin direction, with increased uncertainty along another) and then returning to a simple CSS. We again emphasize that no significant correlations between the atoms are induced by these dynamics, but nonetheless, correlations of the (single-atom) spin distributions along the different spin projection axes can be induced by the nonlinear J_z^2 term. To characterize this behavior, we directly measure the spin distributions along the different spin directions J_x , J_y , and J_z . We combine these measurements to determine the spin length

$$L = \frac{\langle J_x \rangle^2 + \langle J_y \rangle^2 + \langle J_z \rangle^2}{J^2} \quad (4)$$

of our artificial spin. For initial CSSs, the length of the spin vector is J , and the spin length is 1, and these properties would be unchanged by simple linear rotations. When the net length of the spin vector becomes zero, the spin length L takes a value of zero. In Fig. 4(d) we show the dependence of the spin length L with increasing effective evolution time τ , i.e., as the parameter $\alpha \equiv \alpha_0 \tau / \hbar$ increases. These measurements

were carried out for two different initial states: the CSS $|\theta = \pi/2, \phi = -\pi/2\rangle_{\text{CSS}}$ and the J_z eigenstate $|J = 2, m_J = 0\rangle_z$.

The y -basis spin dynamics of the initial CSS are shown in Fig. 4(a). Initially aligned along the $-y$ axis (at $\alpha = 0$), the CSS [red squares in Fig. 4(d)] should have a spin length of 1. In experiment, imperfections in the state preparation and measurement rotations cause deviation of the measurements at $\alpha = 0$. At a larger effective evolution time ($\alpha = \pi/2$), the spin has rearranged itself such that half of the probability density is concentrated on each of the $-y$ and $+y$ axes [Fig. 4(c), left] resulting in a minimum spin length. Later, at $\alpha = \pi$, the spin realigns along the $+y$ axis and forms the state $|\theta = \pi/2, \phi = +\pi/2\rangle_{\text{CSS}}$, as depicted in Fig. 4(c). This process is also demonstrated in the y -basis absorption images shown in Fig. 4(a). We note that the slight offset of the data in Fig. 4(d) is primarily due to an additional phase shift caused by atomic interactions in the synthetic lattice of momentum states (see Ref. [28] for more information).

In contrast to these dynamics of the CSS, the J_z eigenstate $|J = 2, m_J = 0\rangle_z$ is entirely unaffected by the J_z^2 operation, as by definition this state can support no important relative phase structure. This independence is illustrated by the data shown in Fig. 4(b), where the y -basis absorption images reflect no change across the entire range of α values. Likewise, as seen in Fig. 4(d) (blue dots), the spin length of this non-CSS remains fixed at $L = 0$ for all values of the effective evolution time α .

While the initial CSS and non-CSS show wildly disparate dynamical behavior in their spin lengths under the nonlinear spin Hamiltonian, they surprisingly behave quite similarly when considering instead the evolution of their out-of-time-ordered correlation functions (OTOCFs) [29]. These functions have been proposed as a suitable measure of dynamically generated entanglement and the scrambling of information in complex, many-body systems [27,30,31], possibly even serving as a probe of many-body localization in disordered systems with interactions [32,33]. Recently, OTOCFs have been measured in ion-based systems [34,35] and in nuclear

magnetic resonance systems [36,37]. Here, we use the wide tunability of our synthetic lattice parameters to measure OTOCFs with an atomic quantum gas. In particular, we demonstrate the suitability of this measure for tracking the complex evolution of arbitrary initial states, including non-CSSs.

Essentially, OTOCFs probe the overlap between an initial state and that same state after some complex evolution characterized by a series of forward- and reverse-time operations. Following the terminology of Ref. [27], we define the OTOCF as

$$F(\alpha) = \langle W_\alpha^\dagger V^\dagger W_\alpha V \rangle, \quad (5)$$

where

$$W_\alpha = U(-\alpha)WU(\alpha) \quad (6)$$

and

$$U(\alpha) = e^{-i\alpha J_z^2} \quad (7)$$

for commuting operators W and V , which we set to be $W = V = e^{-i\frac{\pi}{4n}J_x}$. We perform the J_z^2 operations with an effective evolution parameter α as described above. Each of the V and W_α operations involves tunneling for a time equivalent to a $\pi/4$ rotation, such that the full experimental duration (ignoring state preparation and readout) is equivalent to that of a global π pulse. For a given initial state $|\Psi\rangle$, we measure $|F(\alpha)|^2$ by first applying the operator $F(\alpha)$ (by stepwise Hamiltonian evolution realizing the operators V , W_α , V^\dagger , and W_α^\dagger), then rotating to a measurement basis in which $|\Psi\rangle$ is an eigenstate, and finally determining the fraction of the condensate wave function which overlaps with the initial state $|\Psi\rangle$. The OTOCF distinguishes between regular and chaotic dynamics by exhibiting exponential decay under chaotic conditions. In the large-spin limit, the exponential decay of OTOCFs under chaotic conditions can be related to the Lyapunov exponent of the associated classical map [38]. Here, we expect that the numerical value of the OTOCF will generally be near 1 if simple, regular dynamics occur [perfect overlap $|F(\alpha=0)|^2 = 1$ if there is no dynamical evolution] and nearer to zero if complex dynamics take place (somewhat similarly to the behavior of the spin length L).

In Fig. 5 we measure the OTOCF under evolution of our squeezing Hamiltonian for the same two initial states discussed previously: $|\theta = \pi/2, \phi = -\pi/2\rangle_{\text{CSS}}$ and $|J = 2, m_J = 0\rangle_z$. In the case of an initial CSS [Fig. 5(a)], the effective squeezing dynamics reflect those seen in the spin length, with $|F(\alpha)|^2$ taking a maximum value at $\alpha/\pi = \{0, 1, 2\}$. For an initial non-CSS, however, while the spin length was completely invariant as a function of α , the OTOCF measurement in Fig. 5(b) shows complex nontrivial dynamics. Thus, the OTOCF serves as a suitable probe for complex dynamics of the underlying Hamiltonian for more general initial states.

We note that the deviations between data and theory in the case of Fig. 5(a) (especially for $\alpha = 0$ and π) cannot be explained solely by incorrect pulse timing stemming from tunneling rate instabilities (which are approximately 4%). Rather, these deviations are due primarily to the loss of coherence between the sites of the synthetic lattice due to increasing spatial separation of the different momentum states. Since the state $|\theta = \pi/2, \phi = -\pi/2\rangle_{\text{CSS}}$ requires a

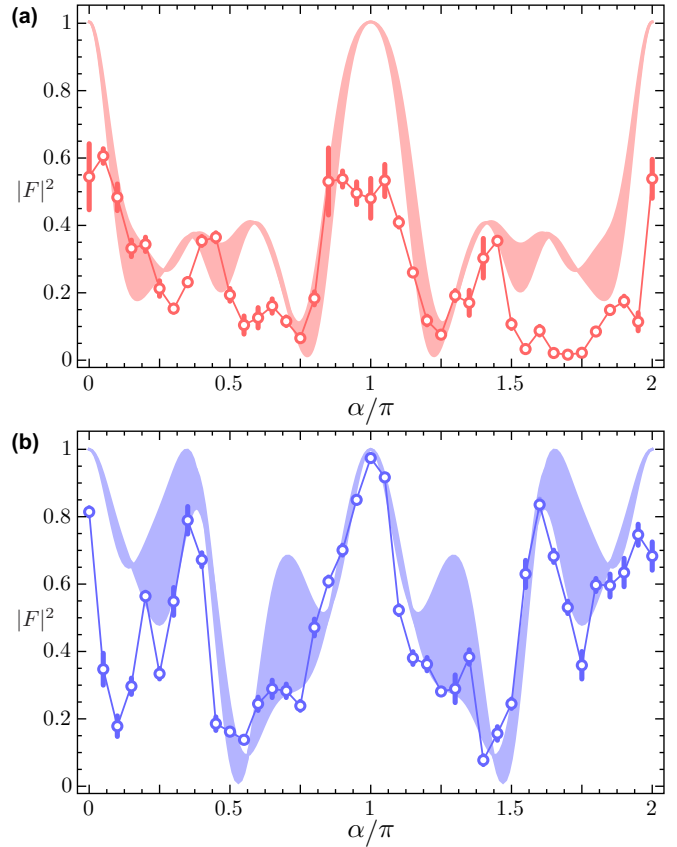


FIG. 5. Out-of-time-ordered correlation function. $|F|^2$ for initial states (a) $|\theta = \pi/2, \phi = -\pi/2\rangle_{\text{CSS}}$ and (b) $|J = 2, m_J = 0\rangle_z$ as a function of the effective dynamics time α . Shaded regions indicate the results of numerical simulations incorporating the uncertainty in the calibrated tunneling rate. All error bars are one standard error of the mean.

state preparation and readout pulse, the momentum states have more experimental time to separate than in the case for $|J = 2, m_J = 0\rangle_z$, where a state preparation and readout is not necessary. This conclusion is supported by Fig. 5(b), which shows much better agreement between theory and data for the initial state $|J = 2, m_J = 0\rangle_z$ than for $|\theta = \pi/2, \phi = -\pi/2\rangle_{\text{CSS}}$. Additionally, we have verified through numerical simulations, including mean-field effects, that the deviations between data and theory in Fig. 5(a) for $\alpha = 0$ and π are not caused by coherent interactions. We find that including mean-field effects in our simulations at the level appropriate for our system only slightly changes the expected result in a way that is not qualitatively important for the present work.

B. Chaotic behavior in the kicked-top model

Having demonstrated all of the necessary ingredients to simulate kicked tops with our artificial spins, we now engineer the full kicked-top model and use it to explore unique aspects of chaotic behavior in a well-controlled quantum system. For different initial CSSs and spin sizes J , we study the spin length following evolution under Eq. (1). In Fig. 6(a), for a spin size $J = 2$ and the initial state $|\theta = \pi/2, \phi = -\pi/2\rangle_{\text{CSS}}$, we show the dynamics of the spin length as a function of the

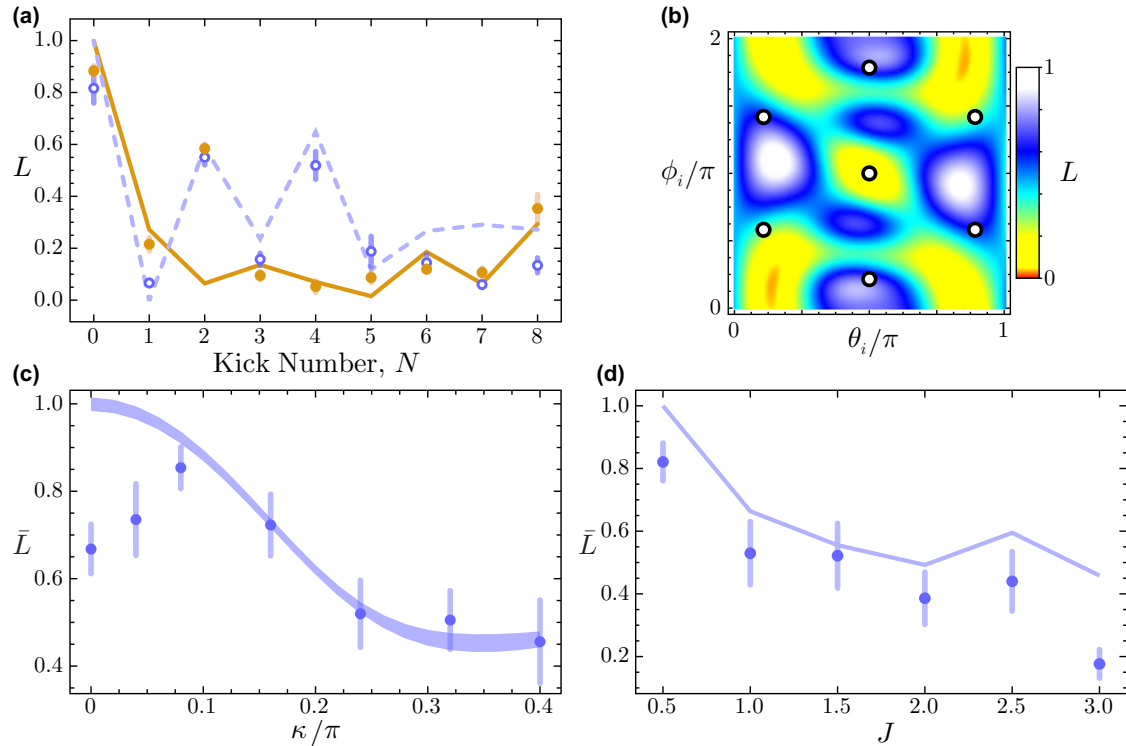


FIG. 6. Chaotic behavior in the kicked-top model. (a) Spin length L for initial state $|\theta = \pi/2, \phi = -\pi/2\rangle_{\text{CSS}}$ measured after each kick in a set of eight kicks. The open blue dots and dashed blue simulation line are $(\rho, \kappa/2J) = (\pi/8, \pi/5)$, and the closed orange dots and solid orange simulation line are $(\rho, \kappa/2J) = (\pi/8, \pi/2)$. (b) Simulated spin length of the effective spin for different initial states. The color represents spin length averaged over $N \in \{5, 6\}$ kicks, with respect to the color bar at right. The seven open black dots represent the measurements taken to calculate the averaged spin length \bar{L} . (c) \bar{L} as a function of the kick strength κ for $(\rho, J) = (\pi/8, 2)$. Shaded regions indicate results from a numerical simulation incorporating the uncertainty in the calibrated tunneling rate. (d) \bar{L} as a function of the size of the spin J for $(\rho, \kappa/2J) = (\pi/8, \pi/2)$. The solid line connects points obtained from a numerical simulation. All error bars are one standard error of the mean.

number of applied kicks. Evolution under two different sets of kicked-top parameters is shown: the solid orange circles relate to $(\rho, \kappa/2J) = (\pi/8, \pi/5)$, and the open blue circles relate to $(\rho, \kappa/2J) = (\pi/8, \pi/2)$. In both cases, the spin length almost immediately decreases to near minimum after a single kick, showing the chaotic nature of the system under these conditions.

Our realization of the quantum kicked-top model allows us to access the complete range of nonlinear coupling strengths with no deleterious side effects. This is in contrast to studies with cesium atoms [12] and with superconducting qubits [21], where only limited ranges of kick strength were explored. Using this full control of κ , we explore the onset of chaotic behavior as the nonlinear coupling strength κ is increased. Because the presence of chaotic behavior in the system is very sensitive to the initial state and because the classical phase-space boundaries (in terms of ϕ and θ) between stable islands and chaotic regions change with increasing κ , we seek to reconstruct a global picture of how a typical initial state would evolve under given kicked-top parameters. As such, we sample seven representative initial CSSs $|\theta = \theta_i, \phi = \phi_i\rangle_{\text{CSS}}$ spread throughout phase space [illustrated in Fig. 6(b)] and measure the spin length averaged over these different cases. Moreover, to account for the fact that the dynamics of L for a given orbit do not necessarily reach some constant value independent of the kick number but in general undergo a

complex evolution, we additionally average over the measured spin length L for five and six kicks. The averaged (over initial state and kick number) spin length \bar{L} is plotted as a function of nonlinear coupling strength κ in Fig. 6(c). A general agreement with the theoretical prediction (solid line) is observed, with a steady decay towards a smaller spin length for increasing κ , signaling the onset of chaotic behavior. For small values of κ the discrepancy between the theory and the data may be due to the lack of tunneling stability in our system (of approximately 4%), which causes incorrect pulse timing, leading to an accumulation of error following many kick periods, state preparation, and state readout.

Finally, we use our unique ability to tune the size of our artificial spin to explore the initial crossover from the fully quantum regime towards the onset of classically chaotic behavior. For increasing J values, where the initial CSSs become more and more sharply defined in terms of their J_x , J_y , and J_z expectation values (normalized to J), one expects to reach a point where classical-like sensitivity to initial conditions can manifest even in quantized systems. A general correspondence between the onset of classical chaos and the development of high entanglement entropy in a quantum system has been observed for systems as small as $J = 3/2$ [21]. Likewise, in the related chaotic system of kicked rotors, classical diffusive behavior has been observed for quantum systems of just two interacting rotors [9]. In Fig. 6(d), we look

at the decay of the averaged spin length \bar{L} for a wide range of J values from $1/2$ to 3 for the case of $(\rho, \kappa/2J) = (\pi/8, \pi/2)$. For the smallest case of $J = 1/2$ the spin should remain in a state with unity spin length at all times and for all initial states. As the system size grows, however, theoretical calculations (solid line) predict a steady trend towards smaller averaged spin length, signaling a crossover to increasingly classical-like chaotic behavior. We indeed observe a similar trend in the dynamical evolution of our artificial spins, with mostly regular evolution for small J giving way to significantly smaller spin length for larger J .

III. DISCUSSION

Our study based on Hamiltonian engineering in a synthetic lattice offers an approach to exploring the correspondence between quantum and classical dynamics, offering the possibility of directly tuning the size of a driven synthetic spin. Here, we have been limited to exploring only modest values of J due to the increasing duration required for rotations of the effective spin for increasing J values. However, straightforward improvements to our experiment should allow us to probe signatures of chaos in artificial spins of size $J \sim 10$ – 20 . Currently, we believe we are limited primarily by the spatial separation of the wave packets related to the many discrete momentum orders. This loss of near-field coherence may be mitigated in the future, however, by creating more spatially extended condensates or through refocusing (echo) protocols.

Our demonstration of a synthetic lattice approach to kicked-top studies also suggests that related platforms, having similar levels of local and dynamical parameter control, could also be used to explore quantum chaos. In particular, the high degree of control in discrete photonic systems [39] should enable similar explorations, perhaps with extensions to much larger effective spin sizes.

In addition to the tunable size of our spins, the wide control afforded by synthetic lattice techniques should also enable further studies on the dynamics of modified kicked tops belonging to distinct symmetry classes [40]. Going beyond the somewhat artificial construction of a synthetic spin, this system also allows for generic studies of Floquet systems. In particular, for regimes in which the atomic interactions are important [28], this system can be used to probe Bose-Hubbard Floquet dynamics. Synthetic lattices should even enable the precise implementation of random unitary operations at the single-particle level. This raises the interesting prospect of exploring boson sampling problems [41] with few-particle Fock states in synthetic lattices.

Last, we remark on the influence of atomic interactions on the dynamics in our kicked top. Under present experimental conditions, the tunneling energy t dominates heavily over the mean-field interaction energy of our condensate atoms U (with $t/U \gtrsim 5$), such that we do not expect any large modification of the dynamics compared to noninteracting particles. However, by working at smaller values of t , we can enter the regime where interactions lead to correlated dynamics. That is, cold collisions give rise to an effective nonlinear interaction in the collective spin of many spin- $1/2$ particles [14] (i.e., nonlinear interactions in a momentum-space double well [28]). The use of a synthetic spin, compared to a real spin, also opens up the intriguing possibility of exploring the driven dynamics of a system of many collectively interacting large- J particles, in which the atomic interactions enrich the system with effective spin-spin interactions. In particular, recent studies of double-well momentum-space systems [28] can be easily extended to triple-well systems and beyond.

ACKNOWLEDGMENT

This material is based upon work supported by the National Science Foundation under Grant No. PHY1707731.

-
- [1] F. Haake, *Quantum Signatures of Chaos* (Springer, Berlin, 2001).
 - [2] T. Hogg and B. A. Huberman, *Phys. Rev. Lett.* **48**, 711 (1982).
 - [3] E. J. Galvez, B. E. Sauer, L. Moorman, P. M. Koch, and D. Richards, *Phys. Rev. Lett.* **61**, 2011 (1988).
 - [4] M. Courtney, N. Spellmeyer, H. Jiao, and D. Kleppner, *Phys. Rev. A* **51**, 3604 (1995).
 - [5] F. L. Moore, J. C. Robinson, C. F. Bharucha, B. Sundaram, and M. G. Raizen, *Phys. Rev. Lett.* **75**, 4598 (1995).
 - [6] W. K. Hensinger, H. Häffner, A. Browaeys, N. R. Heckenberg, K. Helmerson, C. McKenzie, G. J. Milburn, S. L. Phillips, W. D. Rolston, H. Rubinsztein-Dunlop, and B. Urcroft, *Nature (London)* **412**, 52 (2001).
 - [7] D. A. Steck, W. H. Oskay, and M. G. Raizen, *Science* **293**, 274 (2001).
 - [8] J.-C. Garreau, *C. R. Phys.* **18**, 31 (2017).
 - [9] B. Gadway, J. Reeves, L. Krinner, and D. Schneble, *Phys. Rev. Lett.* **110**, 190401 (2013).
 - [10] J. L. Bohn, A. V. Avdeenkov, and M. P. Deskevich, *Phys. Rev. Lett.* **89**, 203202 (2002).
 - [11] A. Frisch, M. Mark, K. Aikawa, F. Ferlaino, J. L. Bohn, C. Makrides, A. Petrov, and S. Kotochigova, *Nature (London)* **507**, 475 (2014).
 - [12] S. Chaudhury, A. Smith, B. E. Anderson, S. Ghose, and P. S. Jessen, *Nature (London)* **461**, 768 (2009).
 - [13] M. Neeley, M. Ansmann, R. C. Bialczak, M. Hofheinz, E. Lucero, A. D. O'Connell, D. Sank, H. Wang, J. Wenner, A. N. Cleland, M. R. Geller, and J. M. Martinis, *Science* **325**, 722 (2009).
 - [14] J. Tomkovič, W. Muessel, H. Strobel, S. Löck, P. Schlagheck, R. Ketzmerick, and M. K. Oberthaler, *Phys. Rev. A* **95**, 011602(R) (2017).
 - [15] A. Facon, E.-K. Dietsche, D. Grosso, S. Haroche, J.-M. Raimond, M. Brune, and S. Gleyzes, *Nature (London)* **535**, 262 (2016).
 - [16] E. J. Meier, F. A. An, and B. Gadway, *Phys. Rev. A* **93**, 051602(R) (2016).
 - [17] B. Gadway, *Phys. Rev. A* **92**, 043606 (2015).
 - [18] W. H. Zurek and J. P. Paz, *Phys. Rev. Lett.* **72**, 2508 (1994).

- [19] K. Furuya, M. C. Nemes, and G. Q. Pellegrino, *Phys. Rev. Lett.* **80**, 5524 (1998).
- [20] M. Kitagawa and M. Ueda, *Phys. Rev. A* **47**, 5138 (1993).
- [21] C. Neill, P. Roushan, M. Fang, Y. Chen, M. Kolodrubetz, Z. Chen, A. Megrant, R. Barends, B. Campbell, B. Chiaro, A. Dunsworth, E. Jeffrey, J. Kelly, J. Mutus, P. J. J. O'Malley, C. Quintana, D. Sank, A. Vainsencher, J. Wenner, T. C. White, A. Polkovnikov, and J. M. Martinis, *Nat. Phys.* **12**, 1037 (2016).
- [22] For more detail on the theory and experimental realization of the momentum-space lattice see Refs. [16,17].
- [23] In units of \hbar/t , this time should scale as $(\pi/2)\sqrt{J(J+1)}$ for integer J and $(\pi/2)(J+1/2)$ for half-integer J .
- [24] S. Chaudhury, S. Merkel, T. Herr, A. Silberfarb, I. H. Deutsch, and P. S. Jessen, *Phys. Rev. Lett.* **99**, 163002 (2007).
- [25] A full reconstruction of the density matrix for a spin of size J can be accomplished through measurement in an appropriate choice of $(2J+1)^2 - 1$ bases, allowing for direct visualization in terms of the experimental Husimi- Q distribution [12].
- [26] J. G. Bohnet, B. C. Sawyer, J. W. Britton, M. L. Wall, A. M. Rey, M. Foss-Feig, and J. J. Bollinger, *Science* **352**, 1297 (2016).
- [27] B. Swingle, G. Bentsen, M. Schleier-Smith, and P. Hayden, *Phys. Rev. A* **94**, 040302(R) (2016).
- [28] F. A. An, E. J. Meier, J. Ang'ong'a, and B. Gadway, *Phys. Rev. Lett.* **120**, 040407 (2018).
- [29] S. H. Shenker and D. Stanford, *J. High Energy Phys.* **03** (2014) 067.
- [30] Y. Sekino and L. Susskind, *J. High Energy Phys.* **10** (2008) 065.
- [31] P. Hosur, X.-L. Qi, D. A. Roberts, and B. Yoshida, *J. High Energy Phys.* **02** (2016) 004.
- [32] R. Fan, P. Zhang, H. Shen, and H. Zhai, *Sci. Bull.* **62**, 707 (2017).
- [33] X. Chen, T. Zhou, D. A. Huse, and E. Fradkin, *Ann. Phys. (Berlin, Ger.)* **529**, 1600332 (2017).
- [34] M. Gärttner, J. G. Bohnet, A. Safavi-Naini, M. L. Wall, J. J. Bollinger, and A. M. Rey, *Nat. Phys.* **13**, 781 (2017).
- [35] K. A. Landsman, C. Figgatt, T. Schuster, N. M. Linke, B. Yoshida, N. Y. Yao, and C. Monroe, *Nature* **567**, 61 (2019).
- [36] J. Li, R. Fan, H. Wang, B. Ye, B. Zeng, H. Zhai, X. Peng, and J. Du, *Phys. Rev. X* **7**, 031011 (2017).
- [37] K. X. Wei, C. Ramanathan, and P. Cappellaro, *Phys. Rev. Lett.* **120**, 070501 (2018).
- [38] E. B. Rozenbaum, S. Ganeshan, and V. Galitski, *Phys. Rev. Lett.* **118**, 086801 (2017).
- [39] R. Keil, A. Perez-Leija, F. Dreisow, M. Heinrich, H. Moya-Cessa, S. Nolte, D. N. Christodoulides, and A. Szameit, *Phys. Rev. Lett.* **107**, 103601 (2011).
- [40] M. Kuś, R. Scharf, and F. Haake, *Z. Phys. B* **66**, 129 (1987).
- [41] A. P. Lund, M. J. Bremner, and T. C. Ralph, *npj Quantum Inf.* **3**, 15 (2017).